

Understanding the Role of Electrode Thickness on Redox Flow Cell Performance

Citation for published version (APA):

Muñoz-Perales, V., van der Heijden, M., de Haas, V., Olinga, J., Vera, M., & Forner-Cuenca, A. (2024). Understanding the Role of Electrode Thickness on Redox Flow Cell Performance. *ChemElectroChem*, 11(2), Article e202300380. <https://doi.org/10.1002/celec.202300380>

Document license:
CC BY

DOI:
[10.1002/celec.202300380](https://doi.org/10.1002/celec.202300380)

Document status and date:
Published: 15/01/2024

Document Version:
Publisher's PDF, also known as Version of Record (includes final page, issue and volume numbers)

Please check the document version of this publication:

- A submitted manuscript is the version of the article upon submission and before peer-review. There can be important differences between the submitted version and the official published version of record. People interested in the research are advised to contact the author for the final version of the publication, or visit the DOI to the publisher's website.
- The final author version and the galley proof are versions of the publication after peer review.
- The final published version features the final layout of the paper including the volume, issue and page numbers.

[Link to publication](#)

General rights

Copyright and moral rights for the publications made accessible in the public portal are retained by the authors and/or other copyright owners and it is a condition of accessing publications that users recognise and abide by the legal requirements associated with these rights.

- Users may download and print one copy of any publication from the public portal for the purpose of private study or research.
- You may not further distribute the material or use it for any profit-making activity or commercial gain
- You may freely distribute the URL identifying the publication in the public portal.

If the publication is distributed under the terms of Article 25fa of the Dutch Copyright Act, indicated by the "Taverne" license above, please follow below link for the End User Agreement:

www.tue.nl/taverne

Take down policy

If you believe that this document breaches copyright please contact us at:

openaccess@tue.nl

providing details and we will investigate your claim.

Understanding the Role of Electrode Thickness on Redox Flow Cell Performance**

Vanesa Muñoz-Perales^{+,*^[a]} Maxime van der Heijden^{+,*^[b]} Victor de Haas,^[b] Jacky Olinga,^[b] Marcos Vera,^[a] and Antoni Forner-Cuenca^{*^[b]}

The electrode thickness is a critical design parameter to engineer high performance redox flow cells by impacting the available surface area for reactions, current and potential distributions, and required pumping power. To date, redox flow cell assemblies employ repurposed off-the-shelf fibrous electrodes which feature a broad range of thicknesses. However, comprehensive guidelines to select the optimal electrode thickness for a given reactor architecture remain elusive. Here, we investigate the effect of the electrode thickness in the range of 200–1100 μm on the cell performance by stacking electrode layers in four different flow cell configurations – Freudenberg paper and ELAT cloth electrodes combined with flow-through and interdigitated flow fields. We employ a suite of polarization,

electrochemical impedance spectroscopy and pressure drop measurements together with pore network modeling simulations to correlate the electrode thickness for various reactor designs to the electrochemical and hydraulic performance. We find that thicker electrodes (420 μm paper electrodes and 812 μm cloth electrodes) are beneficial in combination with flow-through flow fields, whereas when using interdigitated flow fields, thinner electrodes (210 μm paper electrodes and 406 μm cloth electrodes) result in a better current density and pressure drop trade-off. We hope our findings will aid researchers and technology practitioners in designing their electrochemical flow cells under convective operation.

Introduction

Large-scale and stationary energy storage technologies are poised to play a notable role in the decarbonization of the electrical sector by facilitating the integration of renewable energy sources in the electricity grid.^[1–3] Redox flow batteries (RFBs) are a promising electrochemical technology for low-cost, scalable and long-duration energy storage.^[4,5] RFBs are rechargeable batteries that electrochemically store energy in redox active species dissolved or suspended in electrolyte solutions housed in external tanks. During operation, the solutions are pumped through an electrochemical stack in which the flow field supplies the electrolyte to the porous

electrode in two distinct half-cells separated by a membrane, to charge or discharge the battery.^[6,7] Their appealing features of decoupling power and energy, high round-trip efficiency, extended durability, and low environmental impact position them ahead of enclosed batteries (e.g., lithium-ion batteries) for large-scale and stationary applications.^[4,8] Despite the technological maturity and advantages of RFBs, their current elevated costs and limited power and energy density have challenged their market penetration and widespread adoption.^[9–11] To increase cost competitiveness and system efficiency, research efforts address technology limitations through the development and engineering of high-performance materials,^[12–16] alternative flow cell designs,^[17,18] new electrolytes^[9,19,20] and improved operational strategies.^[21–23]


At the core of the electrochemical flow reactor, the porous electrode and flow field design determine the battery performance as they both impact the mass and charge transport.^[24] The porous electrodes provide the active surface area for the electrochemical reactions, distribute the electrolyte (affecting species mass transport and pressure drop) and conduct electrons and heat.^[21,25] The electrode performance is governed by their surface chemistry and microstructure, characterized by the pore size distribution (PSD), anisotropy ratio, fiber alignment and pore morphology.^[26–32] As such, authors have studied the role of the electrode microstructure on the electrochemical performance and pressure drop,^[26,33–35] while others have designed and synthesized electrode materials with distinct chemical and physical properties.^[13,30,36] The flow field geometry similarly affects the flow cell performance by controlling the electrolyte distribution and accessibility to the electrode surface area in the porous electrode, electrode compression and cell pressure drop.^[27,37–40] Conventional geometries – flow-through,


[a] Dr. V. Muñoz-Perales,⁺ Prof. Dr. M. Vera
 Department of Thermal and Fluids Engineering
 Universidad Carlos III de Madrid
 28911-Leganés (Spain)
 E-mail: vamunozp@ing.uc3m.es

[b] Dr. M. van der Heijden,⁺ V. de Haas, J. Olinga, Prof. Dr. A. Forner-Cuenca
 Electrochemical Materials and Systems
 Department of Chemical Engineering and Chemistry
 Eindhoven University of Technology
 Eindhoven 5600 MB (The Netherlands)
 E-mail: m.v.d.heijden@tue.nl
 a.forner.cuenca@tue.nl

[⁺] These authors contributed equally to this work.

[**] A previous version of this manuscript has been deposited on a preprint server (DOI: <https://doi.org/10.26434/chemrxiv-2023-n2mmd>)

 Supporting information for this article is available on the WWW under <https://doi.org/10.1002/celec.202300380>

 © 2023 The Authors. ChemElectroChem published by Wiley-VCH GmbH. This is an open access article under the terms of the Creative Commons Attribution License, which permits use, distribution and reproduction in any medium, provided the original work is properly cited.

interdigitated, parallel and serpentine – have been investigated by evaluating their pressure drop and electrochemical performance in RFBs and by computational methods,^[40–45] and have been optimized by engineering their geometric parameters (e.g., channel and rib width)^[46–48] and patterns.^[17,18]

The thickness of the porous electrode plays an integral role in the performance and efficiency of the electrochemical stack. Specifically, the electrode thickness impacts cell overpotentials through electronic and ionic resistances (ohmics), electrolyte distribution and residence time (mass transfer) and available surface area for reactions (kinetics). Furthermore, the pressure loss and resulting pumping requirements are also determined by the electrode thickness.^[49–51] Because of the contradictory nature of some of these properties (i.e., surface area and permeability), finding an optimal electrode thickness is not trivial. An optimal electrode thickness should provide the highest possible electrochemical performance (e.g., higher total surface area given by thicker electrodes) and the lowest possible pumping power required (e.g., lower flow rates are needed to sustain the same electrolyte velocity with thinner electrodes) which strongly depends on the specific reactor architecture and redox chemistry. To date, two predominant electrode thickness ranges have been implemented in RFBs. First, thick felts (1–6 mm in thickness) are a common choice in traditional flow battery designs, benefitting from high surface areas but suffering from bulkier reactors and inhomogeneous compression upon assembly.^[52] As a consequence, contemporary flow cell reactors leverage thinner electrodes (200–600 μm in thickness) which enable more compact stacks, lower cell resistance, reduced pressure drop and easier assemblies due to homogeneous cell compression.^[40,44,53,54] Among the thin electrodes, commercially available carbon papers and cloths have been primarily repurposed from gas diffusion layers in low-temperature fuel cells.^[26,55,56] While these materials are functional, they have not been engineered to fulfill the specific requirements of RFBs, resulting in suboptimal battery performance.

A few groups have investigated the role of the electrode thickness on the flow cell performance.^[53,54,57–60] Aaron *et al.* varied the electrode thickness in each separate half-cell by stacking multiple SGL 10AA carbon paper electrodes (1, 2 or 3 layers) using a serpentine flow field at a constant flow rate of 20 mL min⁻¹. They demonstrated a performance gain in all-vanadium RFBs by stacking electrodes, with an enhanced performance for two electrode layers. While the activation losses were reduced by scaling the available surface area, the ohmic losses conversely affected the system performance.^[54] Similarly, Liu *et al.* analyzed the influence of the electrode thickness of SGL 10AA carbon papers, varying from one to nine layers, in combination with a serpentine flow field evaluated at 20 and 90 mL min⁻¹. They found an optimum in three electrode layers, providing simultaneously high electrochemical performance and low pressure drop. Despite the increase in the electrode reaction volume and the limiting current upon increasing the electrode thickness above three layers, they reported that the resulting high area-specific resistance negatively impacts the overall performance.^[53,61] These studies

revealed the importance of the electrode thickness by studying the specific combination of SGL 10AA carbon paper electrodes with serpentine flow fields at a certain flow rate and electrolyte chemistry. However, previous studies largely overlook the coupled influence of the electrode microstructure and flow field geometry when evaluating the effects of the electrode thickness on the battery performance. As anticipated by previous literature, the local properties within the cell will be affected by the cell architecture, the operating conditions and the redox chemistry.^[7,24,25,35,62] In particular, driven by the different penetration depths of the electrolyte through the electrode and the velocity distribution, the influence of the electrode thickness on the cell performance is expected to strongly depend on the unique flow patterns induced by the type of flow field design used. The available flow pathways in the electrode will correlate to the electrolyte residence time in the electrode, species depletion, surface area utilization and pressure drop. Although previous studies have shown the dependency of the electrode thickness on the flow cell performance, prior findings show that these correlations are highly dependent on the specific electrode type and flow field geometry. Broader design relationships should be elucidated for prominent electrode morphologies, such as bimodal and unimodal microstructures, and flow field geometries, such as flow-through and interdigitated designs, as they would aid in the understanding of relevant structure-performance relationships in the electrochemical cell and thus assist the research on advanced electrode and flow field designs.

In this study, we seek to systematically investigate the correlations between the electrode thickness, electrode microstructure and flow field geometry for four reactor architectures that cover a representative design space of prevalent component choices. The influence of the electrode thickness on the cell performance is investigated by stacking electrode layers (200–1100 μm) of two commercial off-the-shelf porous electrodes – Freudenberg carbon paper and ELAT carbon cloth – in combination with two prevailing flow field geometries – flow-through and interdigitated (Figure 1a). We use flow cells as analytical platforms for the characterization of the electrochemical and fluid dynamic performance together with a pore network model to gain insight into the local properties to help elucidate thickness-structure-performance relationships. First, we quantify the pressure losses through all electrode-flow field combinations using a custom setup and extract their electrode-flow field apparent permeabilities. Second, we evaluate the electrochemical performance in a single electrolyte flow cell (Figure 1b) using a kinetically facile redox couple (Fe²⁺/Fe³⁺) with electrochemical impedance spectroscopy and polarization measurements. In parallel, pore network model (PNM) simulations (Figure 1c) are performed to shed light on the local profiles sustained under the experimental performance of the battery, capturing fluid dynamics, current density and concentration profiles in the porous electrode. The model was previously developed and validated for paper and cloth electrodes with flow-through configurations^[35] and is extended in this work to an interdigitated flow field configuration. Finally, we analyze the electrochemical and pressure drop trade-offs for

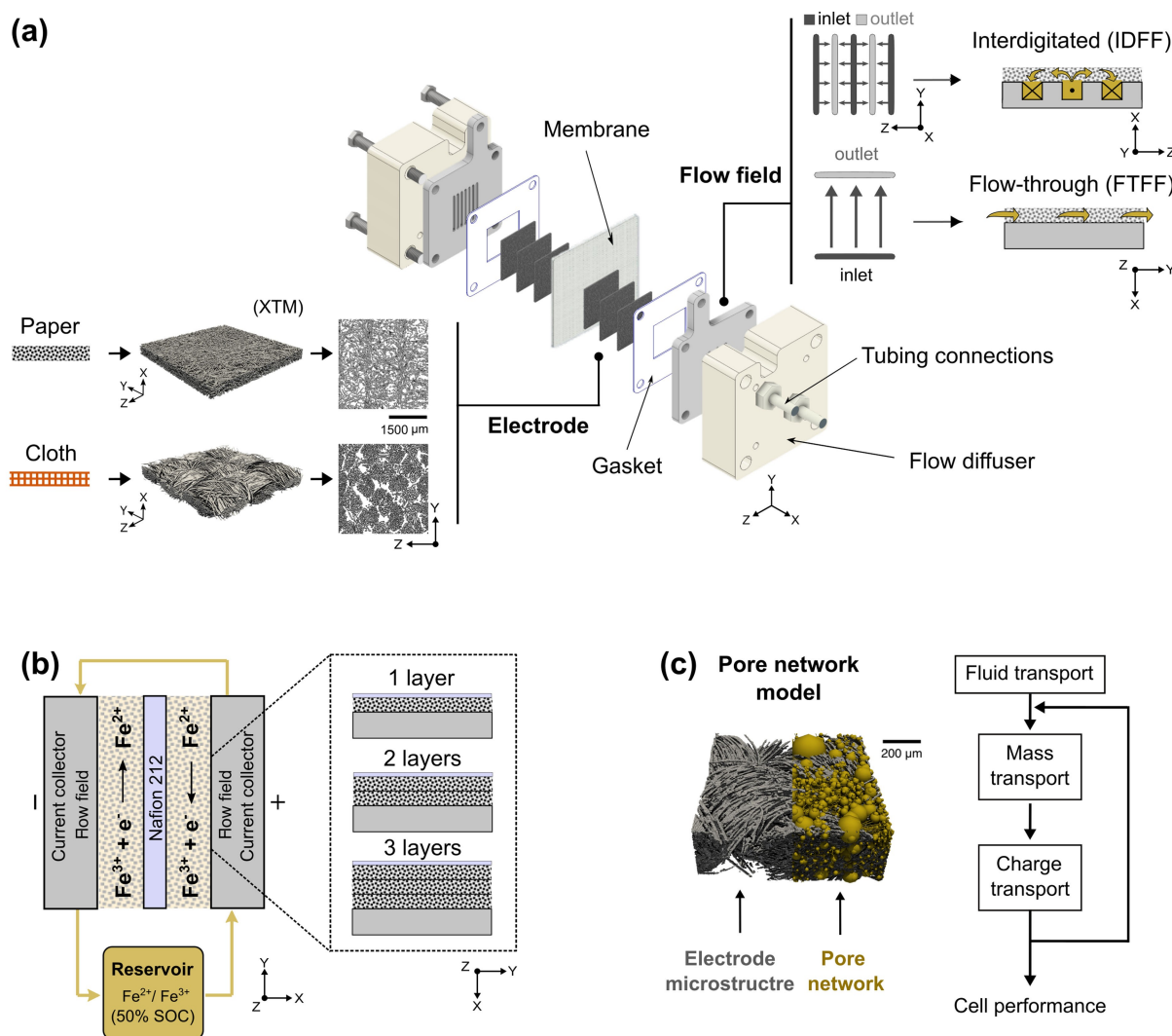


Figure 1. Schematic representation of the outline of this work. (a) The flow cell configuration with the individual cell components,^[63] including the two flow field designs (flow-through and interdigitated) and the two electrode structures (carbon paper and cloth) with the 3D renderings and in-plane cross-sections obtained with X-ray tomographic microscopy.^[24] (b) The single-electrolyte cell configuration with a 0.1 M FeCl_2 , 0.1 M FeCl_3 in 2 M HCl electrolyte solution together with a visualization of the stacked electrode layers used for the electrochemical experiments. (c) The electrode microstructure of the cloth electrode (obtained by X-ray tomographic microscopy) overlaid with the resulting pore network, and the simplified iterative flowchart of the model.

stacked electrodes for every electrode-flow field configuration. Our findings highlight the need for co-designing the electrode thickness, electrode microstructure and flow field geometry to enhance flow cell performance. While we employ laboratory-scale cells in this study, we anticipate that these results can be used as a guideline to select and design electrodes and flow fields for emerging flow cell reactors.

Experimental Methods

Materials

Two commercial porous carbon-fiber electrodes were investigated in this work: a Freudenberg H23 carbon paper (Fuel Cell Store) and an ELAT carbon cloth (Fuel Cell Store), hereafter referred to as paper and cloth, respectively. Freudenberg H23 is a non-woven and binder-free paper electrode with an uncompressed thickness of

210 μm and a porosity of 80%, whereas the ELAT cloth is a periodically ordered structure featuring a plain weave pattern with a thickness of 406 μm and a porosity of 82%.^[26] Both electrodes were pre-treated by thermal oxidation in air at 450 $^\circ\text{C}$ for 12 h (in a Nabertherm muffle oven, model C290) to increase the hydrophilicity of the electrode to facilitate complete electrode wetting.^[64] The geometrical area of the electrodes used in the flow cells was 2.55 cm^2 . The two different flow fields used in this work - flow-through and interdigitated - were milled from graphite plates (G347B Plate, MWI). The flow-through flow field (FTFF) had one inlet and one outlet channel of 14 \times 1 mm^2 , separated by a 16 mm long rib, whereas the interdigitated flow field (IDFF) had 4 inlet channels and 3 outlet channels of 16 \times 1 mm^2 , alternating with 1 mm wide ribs. A Nafion 212 cation exchange membrane (Fuel Cell Store, 50.8 μm) was used to separate both half-cells and was pre-treated by immersion in 2 M hydrochloric acid (37% w/w HCl diluted in deionized water) for at least 3 days. The electrolyte used for the electrochemical experiments was prepared by dissolving 0.1 M ferrous chloride hydrate ($\text{FeCl}_2 \cdot 4\text{H}_2\text{O}$, 98%, Sigma-Aldrich) and

0.1 M ferric chloride hydrate ($\text{FeCl}_3 \cdot 6\text{H}_2\text{O}$, 97%, Sigma-Aldrich) in 2 M HCl at ambient temperature.

Pressure Drop Measurements

The pressure drop through the flow cell configurations was measured in a custom flow cell setup (Figure S1). Water was pumped through the flow cell using a peristaltic pump (Masterflex L/S(R) Easy-Load(R) II) and LS-14 tubing, where only one side of the cell was connected to the solution reservoir. For simplicity, water was used as it has similar density, viscosity, surface tension and wetting properties as the aqueous electrolyte due to the low species concentration.^[65] The flow cell was tightened to 2 N m with a torque-controlled screw-driver and consisted of two flow diffusers, machined from polypropylene (McMaster-Carr), one graphite current collector milled with a flow field design from 3.18 mm thick resin-impregnated graphite plates (G347B graphite, MWI, Inc.)^[66] (vide supra), 1–3 electrodes with incompressible polytetrafluoroethylene gaskets (ERIKS, 210 μm , 105 μm and 55 μm in thickness) that control the electrode thickness by applying a compression of ~20% (where the total gasket thickness depended on the electrode thickness. The exact compression values can be found in Table S1), and a dense aluminum plate to ensure that the pressure drop was measured over only one flow field and one electrode to avoid secondary effects such as membrane crossover. To account for the different electrode thicknesses throughout the manuscript, we chose to perform the measurements at a constant electrolyte velocity, rather than at a constant flow rate. Using this approach, the electrolyte velocities in the porous electrodes are comparable and allow for a meaningful comparison of mass transport properties between the distinct electrode structures, flow field designs and number of stacked electrodes. To this end, the electrolyte solution was pumped through the cell at a flow rate calculated based on the desired electrolyte velocity in the electrode ($v_e \sim 0.5\text{--}8 \text{ cm s}^{-1}$, see equations S1–S2 in Section S2). For all flow cell experiments, the same pre-conditioning procedure was followed, consisting of a pump calibration step at 5 cm s^{-1} followed by pumping the electrolyte solution through the cell for 30 min at 5 cm s^{-1} . The experiments were performed starting with the highest velocity (8 cm s^{-1}) in descending order to improve the electrode wetting, and the pressure was measured at the inlet and outlet with digital pressure gauges (Stauff SPG-DIGI-USB).

The pressure drop per unit length of the electrode was correlated to the electrolyte velocity using the Darcy-Forchheimer equation [Eq. (1)]:

$$\frac{\Delta P}{L} = \frac{\mu}{k} v_e + \beta \rho v_e^2 \quad (1)$$

where ΔP is the pressure drop (Pa), L the length of the electrode (m), v_e the electrolyte velocity (m s^{-1}) and μ and ρ are the electrolyte viscosity (Pa s) and density (kg m^{-3}), respectively. In this study, we refer to k as the apparent permeability (m^2) and to β as the apparent Forchheimer coefficient (m^{-1}) that accounts for inertial effects. Because both the permeability and Forchheimer coefficient are intrinsic properties of the porous material, we refer to them as “apparent” in this work to account for the coupled hydraulic properties of the electrode-flow field combination. All measurements were repeated twice ($n=2$) for new cell assemblies and solutions.

Electrochemical Characterization

The electrochemical performance of every electrode-flow field combination was assessed in a single-electrolyte flow cell (Figure 1b).^[67,68] The single-electrolyte configuration has been used in a variety of previous studies^[63,69] and allows us to directly evaluate the ohmic, activation and mass transfer overpotentials, without convoluted effects such as membrane crossover, secondary reactions and variations in the state-of-charge over time. An $\text{Fe}^{2+}/\text{Fe}^{3+}$ electrolyte at 50% state-of-charge was pumped through the cell by a looped tube design, where the outlet of the first half-cell was connected to the inlet of the second half-cell. Once the system reached stationary conditions after cell pre-conditioning, the desired flow rate to sustain a certain velocity was applied and sequential electrochemical impedance spectroscopy (EIS) and polarization measurements were performed using a Biologic VMP-300 potentiostat. EIS was performed at open circuit voltage, with a 10 mV amplitude over a frequency range from 10 kHz–50 mHz, 6 points per decade, 3 measurements per frequency and a waiting time of 0.1 period before each frequency. To deconvolute the ohmic, activation and mass transfer resistances, an equivalent circuit model^[70,71] was used to fit the averaged experimental values (see Section S3). The model consists of an inductor (L) capturing the lead resistance, in series with an ohmic resistor (R_Ω), as well as a constant-phase element (CPE₁), representing the non-ideal capacitive effects of porous electrodes,^[72] in parallel with a charge transfer resistor (R_{CT}), in series with a second constant-phase element (CPE₂), in parallel with a mass transfer resistor (R_{MT}). The second CPE captures inhomogeneities in current and potential distribution, surface reactivity and porosity, which are common features in porous electrodes.^[73] Polarization measurements were obtained by applying potentiostatic holds of 1 min at constant voltage steps of 10 mV between 0–0.2 V and by recording the steady-state current (one point per second, where only the last 20 seconds were averaged). Because a single-electrolyte configuration was used, the same but opposite reactions occur in both half-cells, resulting in an open circuit voltage of 0 V. Therefore, the applied potential corresponds to the cell overpotential, comprising the ohmic, activation and mass transfer resistances.^[26] All experiments were repeated at least twice ($n \geq 2$) for new cell assemblies and electrolyte solutions.

Electrolyte Conductivity and Membrane Resistance Measurements

To improve the accuracy of the pore network model simulations, the electrolyte conductivity and membrane resistance were determined experimentally. Conductivity measurements were performed using a two-electrode custom conductivity cell (similar to the setup used in Milshtein *et al.*^[74]), where the open compartment of the conductivity cell was filled with the electrolyte solution and sealed shut. EIS was performed at open-circuit voltage and room temperature with an amplitude of 10 mV and a frequency range of 20 kHz–200 mHz, 8 points per decade, 6 measurements per frequency and a waiting time of 0.10 period before each frequency. The high-frequency intercept was identified as the value of the total resistance (cell, lead and electrolyte resistance) and a calibration curve was obtained using aqueous conductivity standards (0.01 M, 0.1 M and 1.0 M aqueous potassium chloride) which, together with an empty cell measurement, was used to correct for the combined cell and lead-resistances. EIS measurements were performed three times for the same solution and were repeated five times ($n=5$) for new assemblies and fresh electrolytes.

To obtain the membrane resistivity, EIS measurements were performed at open-circuit voltage where the high-frequency intercept was identified as the cell resistance including e.g., the

membrane resistance and electronic contact resistances. The membrane resistance was obtained by correcting for a cell without a membrane (regular flow cell configuration but without the membrane) and was measured for every electrode-flow field combination with one electrode layer (see Table S6). Because of the nature of this experiment, the contact resistance contribution to the measured membrane resistance was minimal (both the measurement with and without membrane have a similar electrode-flow field contact resistance and was thus corrected for). EIS measurements were performed for five velocities (20, 10, 5, 3.5 and 1.5 cm s^{-1}) and were repeated two times ($n=2$) for new membranes, electrodes, and cell assemblies. The obtained values were used in the PNM as membrane resistivity by multiplying the membrane resistance by the geometrical area of the electrode (2.55 cm^2).

Exchange Current Density Extraction

The exchange current density (j_0 , A m^{-2}), used as an input parameter in the pore network simulations, of each electrode and flow field combination was estimated from the polarization experiments by fitting the low current density region ($< 100 \text{ mA cm}^{-2}$) of the polarization curve to the Butler-Volmer equation (see equation (2))

$$i = j_0 \left(\frac{C_{i,s}}{C_{ref}} \left[\exp\left(\frac{\alpha F}{RT} \eta\right) - \exp\left(-\frac{\alpha F}{RT} \eta\right) \right] \right) \quad (2)$$

where i is the current density (A m^{-2}), $C_{i,s}$ the surface concentration of species i (mol m^{-3}), C_{ref} the reference concentration of the species (mol m^{-3}) at which the exchange current density was measured, α the reaction transfer coefficient (–) which is 0.5 for the $\text{Fe}^{2+}/\text{Fe}^{3+}$ species, F Faraday's constant (96485 C mol^{-1}), R the universal gas constant ($8.314 \text{ J mol}^{-1} \text{ K}^{-1}$), T the operating temperature (298 K) and η_{act} the activation overpotential (V) obtained after iR_{Ω} -correction of the applied potential and assuming mass transfer

overpotentials to be negligible in the low current density region, resulting in $C_{i,s} = C_{ref}$. The exchange current densities were obtained for each electrode and flow field combination (Table S5).

Pore Network Modeling

Pore network models can be leveraged to simulate the local transport within porous electrodes at a low computational cost by assuming the void space within the porous structure to be approximated by spherical pores and cylindrical throats. Because of the simplification of the pore space and inherent assumptions,^[35,67] the PNM should primarily be used to qualitatively obtain and compare property profiles (e.g., concentration, current, velocity, pressure) through the porous electrode while retaining microstructural information. The pore network model used in this study was validated and described in detail in a previous work^[35] and the model equations and iterative scheme can be found in Figure S4. Nevertheless, the model was again validated for all configurations used in this work with experimental data, as the model was extended to simulate the IDFF in this work (Figure 2b). The validation of all configurations is discussed in detail in Section S8, where the experimental data is compared with the unfitted model simulations in Figure S7, the fitted model simulations in Figure S8, the model parameter fitting data in Table S6 and a detailed discussion on the model fitting in Section S8.

The modeled domain consists of two symmetric, mirrored $1 \times 1 \text{ mm}^2$ porous electrodes for the FTFF and $1 \times 2 \text{ mm}^2$ electrodes for the IDFF simulations, obtained by X-ray tomographic microscopy in previous work.^[35] The layer study was performed by stacking the processed uncompressed X-ray tomographic images in the thickness (x) direction in ImageJ to obtain 1, 2 or 3 electrode layers. Subsequently, the pore networks were extracted using the SNOW algorithm, using the inscribed diameter for the paper electrode and the equivalent diameter for the cloth electrode,^[75] where the network extraction was performed using a single Intel® Core™ i5-12500 CPU. Single-electrolyte flow cell simulations (50% state-of-

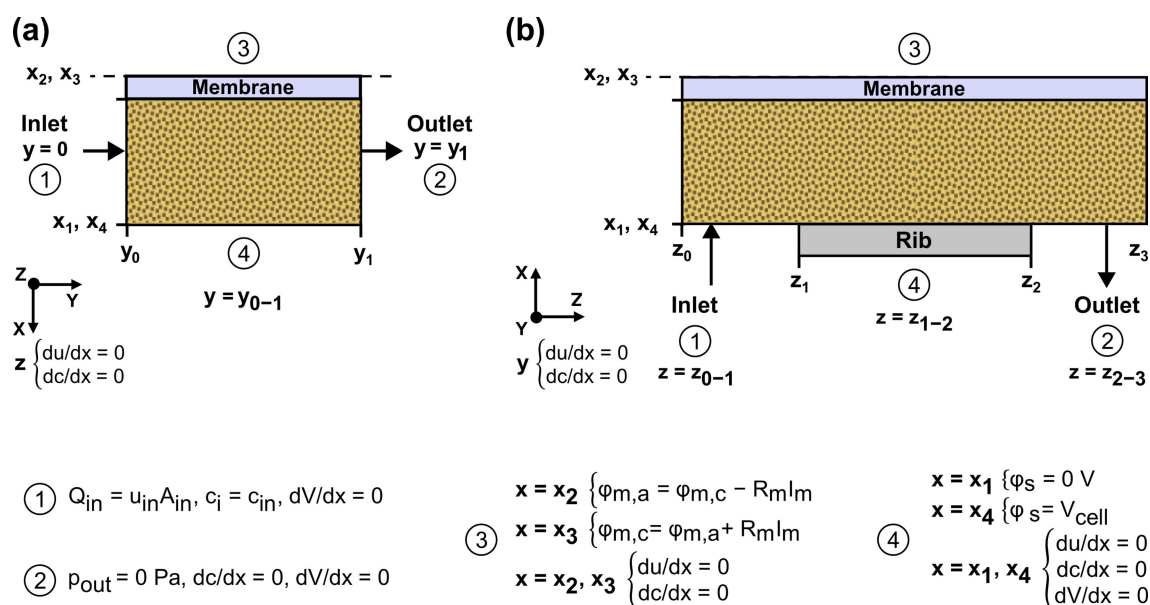


Figure 2. Schematic representation of the boundary conditions used in the electrochemical pore network model for one of the half cells in the single-electrolyte flow cell, with x_1 – x_4 the x -coordinates, 0 – y_1 the y -coordinates, and z_0 – z_3 the z -coordinates of the different interfaces for the: (a) flow-through flow field, shown over the electrode length (y) and thickness (x), and (b) the interdigitated flow field, shown over the electrode width (z) and thickness (x). The flow field and current collector are located on the bottom side of the electrode and the membrane on the top, where the dashed line shows the symmetry condition over the membrane. The symbol list for this figure can be found in Section S12.

charge, open circuit voltage of 0 V, see Table 1 for the model parameters) were conducted with applied negative potentials with co-flow operation of the anodic (oxidation reaction) and cathodic (reduction reaction) half-cells. The transport equations were solved at each pore, and the location of the flow channels and ribs, current collectors and membrane were defined by boundary conditions (Figure 2). The single-electrolyte configuration enables the investigation of the electrode performance in isolation without competitive phenomena such as species crossover through the membrane or variations in the state-of-charge.^[76,77]

The electrochemical PNM framework first solves the fluid transport and consecutively the coupled mass and charge transport within both compartments using an iterative approach. The pressure field was obtained using the Navier-Stokes equation, from which the velocity was back-calculated with the Hagen-Poiseuille equation. These equations can be solved independently from the mass and charge transport equations as a result of the dilute electrolyte used in this study.^[35] Subsequently, the obtained pressure field is fed in the iterative algorithm to solve the coupled mass and charge transport in the porous electrode using the advection-diffusion-reaction equation and the conservation of charge equation. The coupling of these two nonlinear systems of equations is done with the Butler-Volmer equation to obtain the species concentration and potential fields. The connection of the half-cells is done at the membrane by only considering the overall macroscopic ionic resistance of the membrane using Ohm's law, resulting in the coupling of the charge transport in one half-cell with the electrolyte potential at the membrane boundary in the other half cell.^[67] Using this approach, experimental contact resistances were not considered in the PNM, which impacts the model validation as described in more detail in Section S8.

To account for species depletion over the length of the electrode for the FTFF system, a network-in-series approach was used to match the length of the laboratory electrode (17 mm). In this approach, pore networks are stitched after one another in the length (y) direction, where each network was rotated to become a mirrored copy (in the flow (y) direction) of the previous network. The concentration at the end of one network was considered the inlet concentration of the next network. Because of the symmetry of the IDFF,^[67] the modeling domain was chosen to be half of an inlet channel, a full rib, and half of an outlet channel, resulting in a $1 \times 2 \text{ mm}^2$ modeling domain for the IDFF simulations, see Figure 2b. For this flow field, species depletion occurs from the inlet channel over the rib to the outlet channel, while species concentration along the channels can be assumed constant.^[78] Thus, a network-in-series approach over the electrode length is not necessary. The computational time to run a 1-layer electrode with the FTFF using

the network-in-series approach and applied potentials of -0.2 – 0 V with -0.02 V step intervals, was 90 min for a $1 \times 17 \text{ mm}^2$ electrode using a single Intel® Core™ i7-8750H CPU. For the IDFF, the same computation took 3 min for a $1 \times 2 \text{ mm}^2$ electrode using a single Intel® Core™ i5-12500 CPU.

The PNM was solved for an applied potential with an initial guess for the concentration and overpotential. The initial guess of the concentration was set to the inlet concentration, whereas the initial guess of the overpotential was 0 V . After the convergence of one network and one applied potential, the initial guesses were updated based on the concentration and overpotential of the converged network. An under-relaxation scheme was imposed on the concentration and potential fields using a constant relaxation factor of 0.1 to counteract solution divergence because of the highly nonlinear nature of the system. Additionally, the charge transport source term was linearized as described in our previous work.^[35] Numerical convergence was achieved when the relative (5×10^{-5}) and absolute ($6 \times 10^{-4} \text{ A cm}^{-2}$) tolerances were met for the total current, bound by a maximum of 50000 iterations.

The boundary conditions for the two flow fields are shown in Figure 2, where the boundary conditions of the IDFF were based on the work of Sadeghi *et al.*^[67] and Shokri *et al.*^[79] The inlet pressure boundary condition is determined by setting a target inlet velocity from which the flow rate is calculated (see equations S1–S2 in Section S2). The inlet pressure at the boundary pores was determined so that the total flow rate entering the network matched the desired flow rate, the discharge pressure was set to zero, and no-flux boundary conditions were imposed at the current collector or rib and membrane regions. A constant inlet concentration of species was imposed at the inlet, and no-flux boundary conditions were applied at the other boundaries. The solid potential at the current collector-electrode interface in the cathodic compartment is equal to the given cell voltage, whereas it is equal to zero in the anodic compartment because of the symmetry of the modeled domain. The electrolyte potential at the membrane is iteratively calculated from the electrolyte potential at the membrane in the other half-cell using Ohm's law, including the average voltage loss across the membrane interface. At the remaining boundaries, no-flux boundary conditions were imposed for the potential.

Table 1. Electrolyte and cell parameters used in the pore network model. ^mExperimentally measured parameter.

Symbol	Quantity	Value
σ_L	Electrolyte conductivity [S m^{-1}]	30.84^m
ρ_L	Electrolyte density [kg m^{-3}]	$1030^{[80]}$
μ_L	Electrolyte viscosity [Pa s]	$1.143 \times 10^{-3}^{[80]}$
$D_{\text{Fe}^{2+}}$	Diffusion coefficient of Fe^{2+} [$\text{m}^2 \text{ s}^{-1}$]	$5.7 \times 10^{-10}^{[81]}$
$D_{\text{Fe}^{3+}}$	Diffusion coefficient of Fe^{3+} [$\text{m}^2 \text{ s}^{-1}$]	$4.8 \times 10^{-10}^{[81]}$
E_{eq}	Equilibrium potential [V]	$0.771^{[6]}$
α_a	Anodic transfer coefficient [–]	$0.5^{[82]}$
α_c	Cathodic transfer coefficient [–]	$0.5^{[82]}$
$C_{\text{Fe}^{2+}}$	Inlet Fe^{2+} concentration in both half-cells [mol m^{-3}]	100
$C_{\text{Fe}^{3+}}$	Inlet Fe^{3+} concentration in both half-cells [mol m^{-3}]	100

Results and Discussion

Pressure Drop Analysis

To correlate the pumping losses of all flow cell configurations, associated with the supply of electrolyte into the electrode,^[58] to the electrode thickness, we first quantify the pressure drop and obtain the apparent permeability from the Darcy-Forchheimer fittings (equation (1)). In Figure 3, the pressure drop per unit length is presented at different superficial velocities, alongside the apparent permeability and Forchheimer coefficient. To sustain the same velocity through the electrode in every electrode-flow field combination, the flow rate needs to increase linearly with the electrode thickness (equation S1–S2). In flow cells utilizing IDFFs, the geometrical inlet area (i.e., electrode thickness multiplied by channel length) for the electrolyte is predefined by the constant area of the flow field channels. Thus, the pressure required for electrolyte ingress through the channel into the electrode is increased upon higher flow rates imposed by thicker electrodes. As a consequence, the results for the IDFF with both electrodes (Figure 3a–b) reveal a proportional increase in pressure drop when more electrode layers are added, evaluated at a constant electrolyte velocity. The increase in pressure drop at a constant electrolyte velocity is further supported by the assessment of the pressure drop at a constant flow rate in Figure S6. At a constant flow rate, no change in pressure losses is observed

when increasing the number of electrode layers with the cloth electrode and only a small decrease is found for the paper electrode. In contrast, FTFF configurations show reverse trends (Figure 3c–d), featuring a substantial decrease in pressure losses, by almost a factor of two, per added electrode layer. In the FTFF configuration, the geometrical inlet area (i.e., channel width multiplied by electrode thickness) increases proportionally to the electrode thickness as the electrolyte flow is supplied from the base of the cell through the transversal cross-section area of the electrode. We would expect that, to sustain a given electrolyte velocity in the electrode the flow rate should increase linearly with the electrode thickness, resulting in a similar required pressure to flow the electrolyte through the porous electrode regardless of the electrode thickness. However, we find that the pressure drop decreases with increased paper electrode thickness for FTFF configurations, which can be attributed to preferential channeling and subsequent hydraulic short-circuiting through the spacing between stacked layers.^[83] The same trends were obtained using the PNM simulations for the FTFF combinations (Table S3); yet, the pressure drop was underestimated for all cases because of the inherent assumptions of PNMs (i.e., the flow resistance through the PNM is attributed to cylindrical throats with a constant circular cross-section, which is a simplification resulting in the underestimation of the pressure drop^[84]) and simulating at uncompressed electrode conditions. Nevertheless, the PNM provides the same

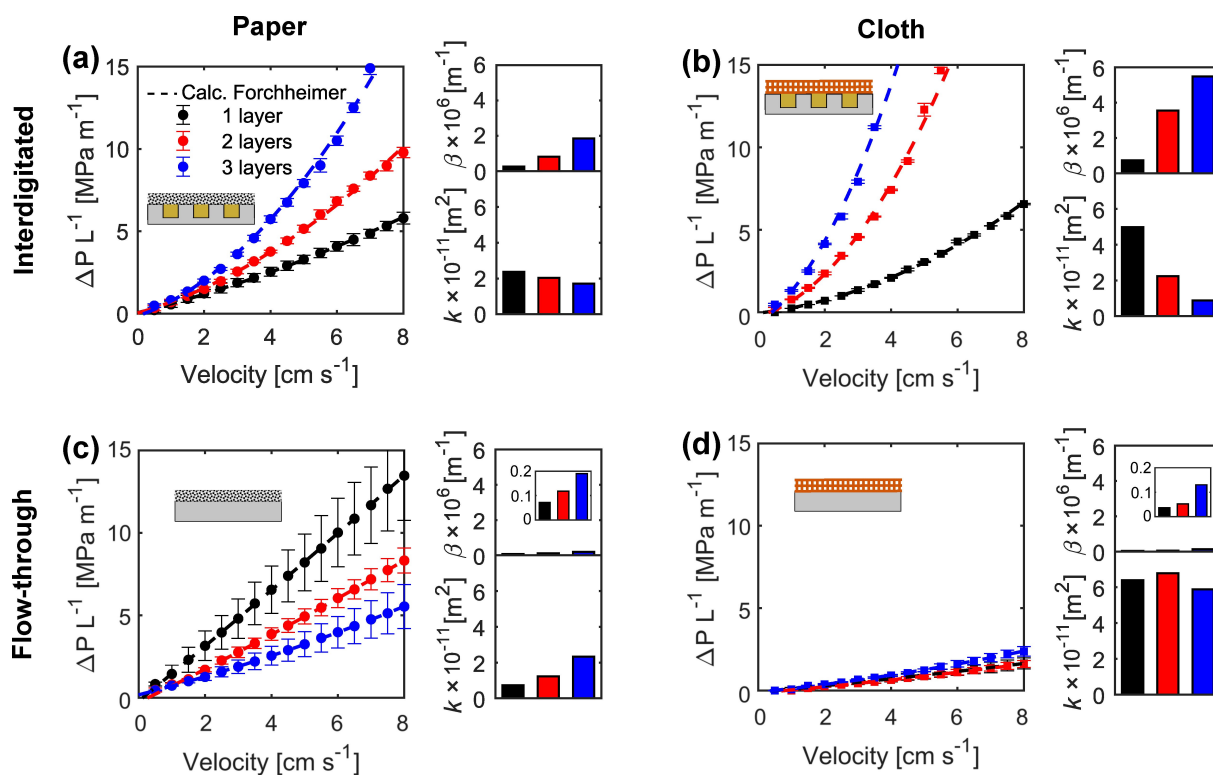


Figure 3. Pressure drop analysis of the four electrode-flow field configurations with 1, 2 and 3 electrode layers. The normalized pressure drop at different electrolyte velocities is presented on the left panel and the apparent permeability and Forchheimer coefficients from the Darcy-Forchheimer fittings on the bottom and top of the right panel, respectively. (a) Interdigitated flow field with the paper electrode, (b) interdigitated flow field with the cloth electrode, (c) flow-through flow field with the paper electrode, and (d) flow-through flow field with the cloth electrode.

trends as observed experimentally, but with additional insights into the microstructural effects on cell operation.

When using IDFF in combination with the paper electrode (Figure 3a), we find a lower pressure drop compared to the cloth electrode (Figure 3b), attributed to the evaluation at constant electrolyte velocity as the paper electrode is twice as thin. Hence, the higher pressure drop of one cloth electrode counterbalances the beneficial effect expected from the higher through-plane apparent permeability (i.e., perpendicular to the membrane, Tables S3–S4) compared to one paper electrode, as observed in Figure 3a–b. Interestingly, the apparent permeability of the cloth-IDFF combinations shows a substantial decrease when stacking electrode layers. We hypothesize that this is a result of electrode compression and the interaction between the cloth microstructure and the flow induced by the IDFF, resulting in both in-plane and through-plane flow within the electrode. Stacking electrode layers can affect the microstructure because of resulting interfacial pores and pore misalignment. In Figure 4, we assess the fluid dynamics of every configuration using the PNM to shed light on the absolute velocity distribution through the throats in the electrode microstructures. When stacking cloth electrodes, the through-plane electrolyte pathways, defined by the large pore segments, are partially blocked because of electrode compression and the fluid is forced to cross the small pores within the fiber bundles. Hence, low liquid permeability and electrode accessibility are attained as illustrated by the non-homogeneous electrolyte distribution in Figure 4b, where the fluid transport predominantly occurs through only a few large in-plane throats with

high absolute electrolyte velocities. The apparent Forchheimer coefficient (Figure 3b) additionally evinces significant inertial effects^[85] caused by the anisotropic microstructure of the cloth electrode, accentuated upon stacking electrodes. At the channel inlet and outlet regions of the IDFF, high electrolyte velocities are sustained, increasing the Reynolds numbers in these regions as well as the inertial effects. The local high-velocity regions are predominantly observed for the cloth electrode, where upon stacking, most of the fluid transport takes place in the electrode layer closest to the current collector. Whereas for the paper electrode, which features a more uniform microstructure,^[26] the apparent permeability and Forchheimer coefficient are not as significantly affected by the addition of electrode layers when using an IDFF. The more homogeneous velocity profiles observed in Figure 4a explain this trend and reveal a better utilization of the paper electrode. In general, for both electrodes (Figure 4a–b), IDFFs induce under-the-rib convection which causes less electrode accessibility under channels.^[41] In addition, in the region adjacent to the membrane, the simulations show lower electrolyte velocities which are expected to exacerbate local depletion, increasing the local mass transfer overpotential near the membrane when the electrode thickness is increased.

By stacking electrodes with a near unimodal PSD (e.g., the paper electrode), additional void space can form between the electrode layers as a result of the mechanical behavior under compressive forces, enhancing the electrode permeability (Figure 3c) in the in-plane direction. When operating using a FTFF, the pressure drop in stacked paper electrodes (from 1 to 3

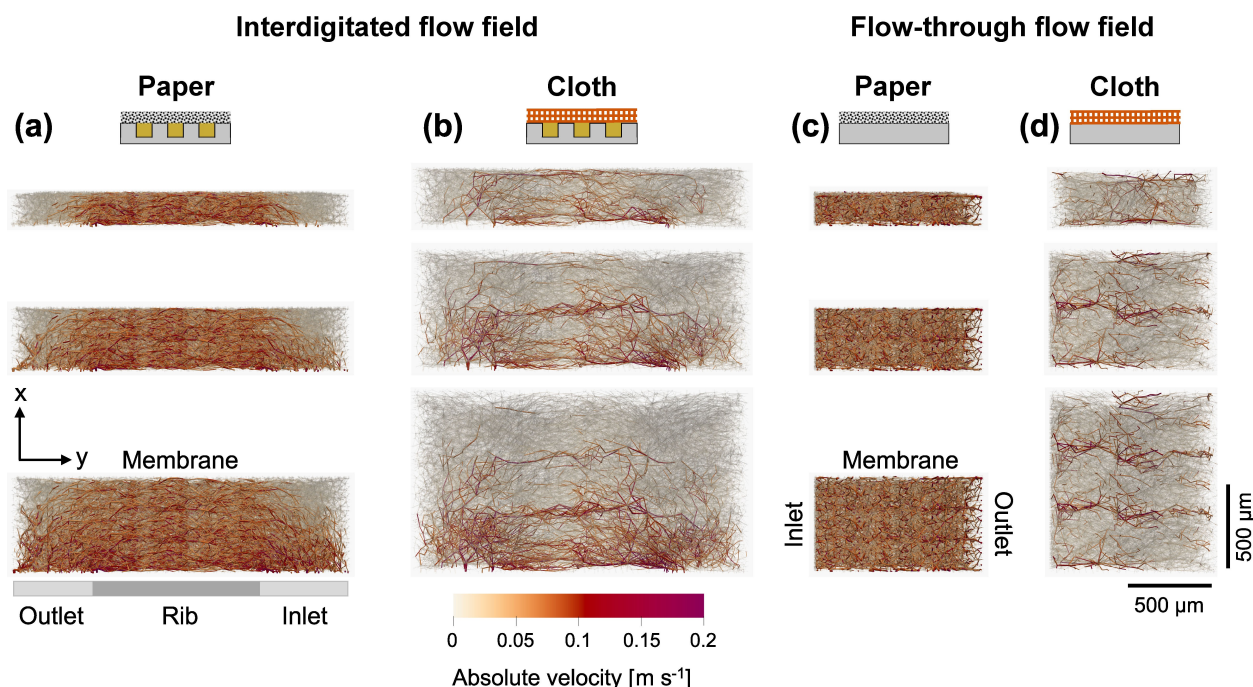


Figure 4. Absolute velocity profiles in the throats obtained with PNM simulations at 3.5 cm s^{-1} in the three-dimensional microstructure of paper and cloth electrodes for the four electrode-flow field combinations: (a) interdigitated flow field with the paper electrode, (b) interdigitated flow field with the cloth electrode, (c) flow-through flow field with the paper electrode, and (d) flow-through flow field with the cloth electrode. The visual representation of the throats does not include the actual throat diameter in the pore network to improve the visibility of the individual throat contributions to the absolute velocity.

layers) is significantly decreased from 13.4 to 5.5 MPa m⁻¹ at $v_e = 8 \text{ cm s}^{-1}$. Despite the seemingly homogeneous velocity distribution in the porous media (Figure 4c), preferential pathways are formed sustaining higher local electrolyte velocities as a result of the inter-layer spacing, decreasing the pressure drop. In the cloth electrode (Figure 3d), no remarkable pressure drop alleviation is observed, which might be due to the obstruction and size reduction of the bimodal pore segments within the microstructure when stacking electrodes (Figure 3d).^[24,35,77] These characteristics provide the cloth-FTFF combination with the lowest pressure losses (<2.5 MPa m⁻¹) among all investigated cell configurations. In general, dominant in-plane convective flow induced with FTFFs leads to small inertial effects, quantified by ten times lower apparent Forchheimer coefficients compared to the hybrid in- and through-plane flow with IDFFs. For example, for the 1-layer case, the paper electrode with a FTFF features a $\beta = 0.2 \times 10^6 \text{ m}^{-1}$ whereas with an IDFF $\beta = 2 \times 10^6 \text{ m}^{-1}$. These small inertial effects could result in less electrolyte mixing, causing a higher mass transfer resistance in flow-through designs.^[63,78,86]

Electrochemical Performance

To evaluate the influence of stacking electrodes on the electrochemical performance, we perform polarization and electrochemical impedance spectroscopy measurements. For all flow cell configurations, the performance is improved when using

stacked electrodes, as shown in Figure 5a–d in the cell polarization plots. However, their trends and magnitude depend on the specific flow field geometry and electrode microstructure, as well as the electrolyte velocity, which in Figure 5 is kept constant at 3.5 cm s⁻¹ (see Figure S10 for other velocities). These differences can be explained by the ohmic, activation and mass transfer overpotential losses in the reactor (Figure 5e–h), and the current distribution through the electrodes obtained with PNM simulations (Figure 6). It should be noted that the cell potential values in this work represent overpotential losses due to the single-electrolyte cell configuration employed; thus, a higher current density at a given cell potential indicates a better performance.

When stacking electrodes in flow cells, the internal surface area increases proportionally to the number of layers, attaining higher current densities by a decrease in both the activation and mass transfer overpotentials,^[76,87,88] as observed in Figure 5. The decrease in activation overpotential is however dependent on the redox chemistry used. Electrolytes featuring sluggish kinetics, such as vanadium (reaction rate constant $\approx 10^{-6} \text{ cm s}^{-1}$ in H₂SO₄^[89]), benefit more of an increased internal surface area compared to kinetically facile electrolytes such as Fe²⁺/Fe³⁺ electrolytes (reaction rate constant $\approx 10^{-3} \text{ cm s}^{-1}$ in HCl and with thermally treated carbon electrodes^[90]) because of the high exchange current density. Furthermore, the mass transfer overpotential is decreased upon electrode stacking as a result of evaluating at a constant electrolyte velocity, resulting in higher mass flow rates and thus enhanced reactant supply for

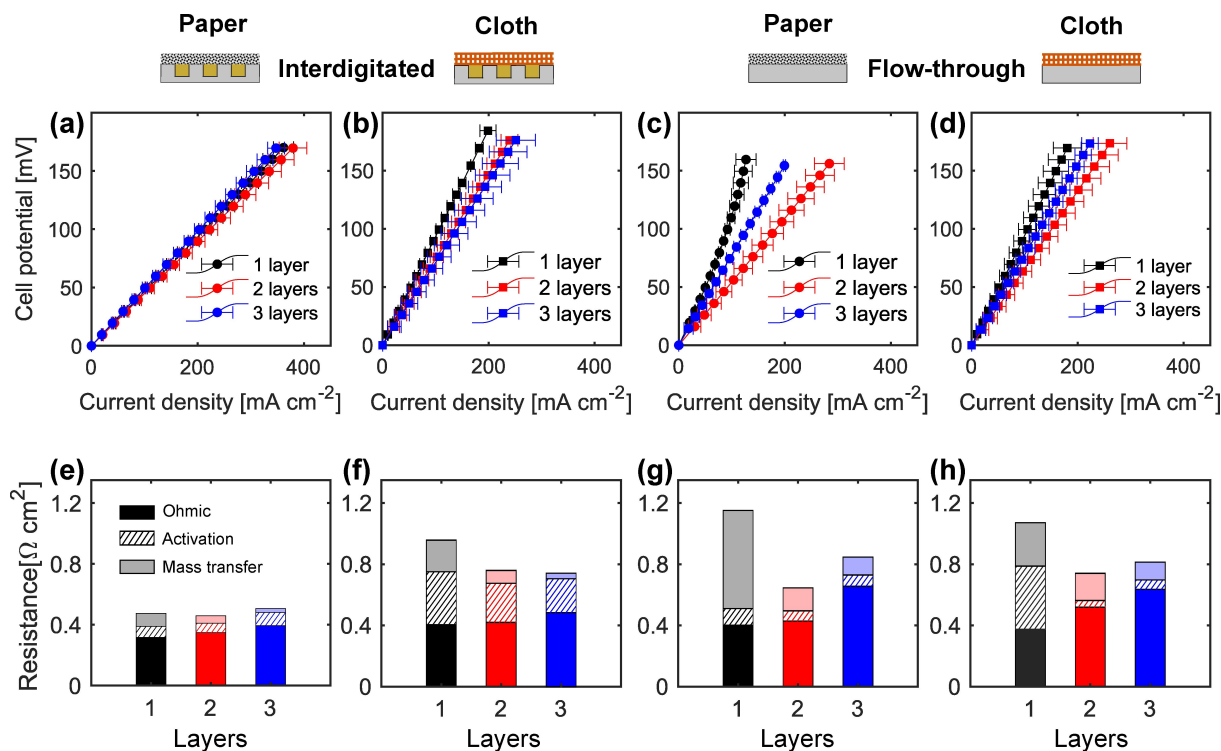


Figure 5. Electrochemical performance of the four electrode-flow field combinations with 1, 2 and 3 electrode layers at 3.5 cm s⁻¹. (a–d) Cell potential vs. current density curves, and (e–h) cumulative addition of ohmic, activation and mass transfer resistances from impedance measurements, for the: (a, e) interdigitated flow field and paper electrode, (b, f) interdigitated flow field and cloth electrode, (c, g) flow-through flow field and paper electrode, and (d, h) flow-through flow field and cloth electrode. The impedance plots can be found in Figure S9.

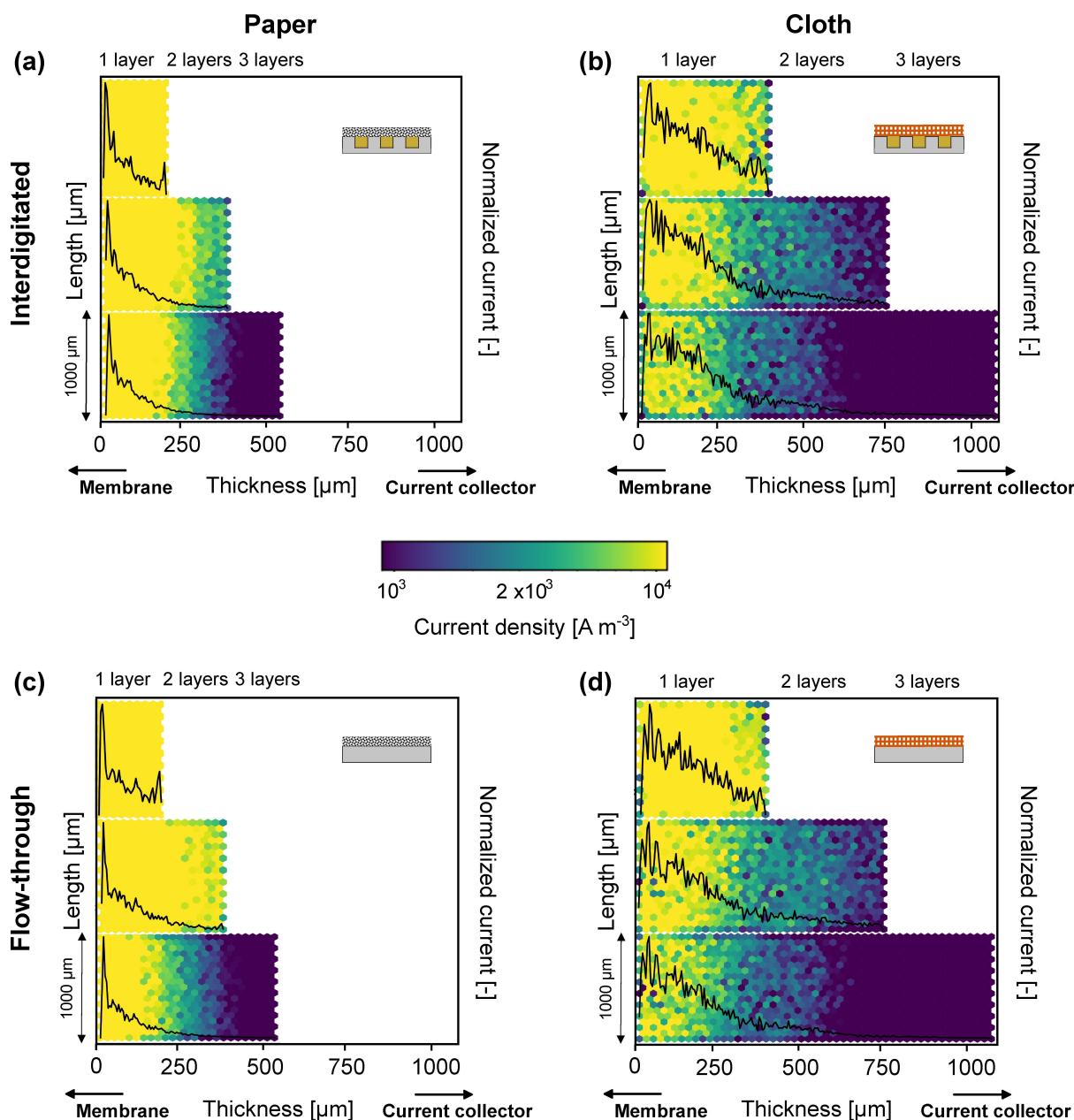


Figure 6. Current profiles in 2D with the current density per volume of electrode plotted over the thickness and length of the electrode, and in 1D with the normalized current (normalized by the total current generated in the electrode) plotted over the electrode thickness, with the membrane at 0 μm. The current profiles are shown for both flow fields and electrodes and for 1, 2 and 3 electrode layers at 3.5 cm s^{-1} and -0.2 V , obtained with pore network simulations, for: (a) the interdigitated flow field and paper electrode, (b) the interdigitated flow field and cloth electrode, (c) the flow-through flow field and paper electrode, and (d) the flow-through flow field and cloth electrode. The validation of the PNM can be found in Section S8.

thicker electrodes. On the other hand, the ohmic overpotential losses increase due to the larger contact (between stacked layers) and ionic resistances which disfavor the ionic transport across thicker electrodes.^[53] Therefore, the reduction in activation and mass transfer resistances is balanced by the higher ohmic resistance, resulting in an optimum for the cell performance at a certain electrode thickness.

In Figure 6, the current distribution profiles in one half-cell are plotted over the electrode thickness and length together with the normalized current values (normalized by the total current generated in the electrode). As observed for all cases,

most of the current is generated near the membrane interface, driven by the high activation and mass transfer reaction overpotentials in that region as a result of greater species reaction rates.^[13,35,91,92] Additionally, the current distribution depends on the fluid dynamics of the system which is impacted by stacking electrodes and gives rise to different velocity profiles and species flux throughout the electrode volume. As a result, even though the addition of layers provides a larger reaction volume for the electrochemical reactions, the non-homogeneous distribution of the current and the low current magnitude obtained in the third layer does not further improve

the electrochemical output of reactors with three electrode layers. As the electrolyte velocity is reduced, the species transport in the cell becomes more diffusion-driven, whereby the ions experience higher residence times to diffuse across the electrode thickness, benefiting less from the preferential pathways originating from high convection (Figure 4). Therefore, flatter current profiles are obtained at low electrolyte velocities (e.g., $v_e = 0.5 \text{ cm s}^{-1}$) and a greater contribution of the total current is generated in the second and third layers (see Figure S11). Furthermore, follow-up studies should investigate the layer thickness of electrode-flow field configurations with various redox electrolyte solutions, as their kinetics and ionic conductivity will influence the ohmic, charge and mass transport potential losses on increasing electrode thickness. For instance, it is anticipated that for highly conductive electrolytes (e.g., aqueous electrolytes with high salt concentration^[93]) the desired electrode layer thickness might be more than two layers, whereas for electrolytes with low conductivity (e.g., organic electrolytes, diluted systems^[74]) one layer might be more beneficial due to the large ohmic losses involved.

Interdigitated Flow Field

For the IDFF, the benefit of adding more electrode layers strongly depends on the electrode type used. The ohmic, activation and mass transfer resistances are significantly influenced by the electrode microstructure and internal surface area due to the complex bidirectional velocity distribution with hybrid in-plane and through-plane flow induced by this flow field design.^[24] As shown in Figure 5e–f, in the paper electrode-IDFF combination, the performance is not further enhanced

upon the addition of more electrode layers, whereas for the cloth electrode the performance is enhanced by stacking two electrodes. Although in Figure 6 a greater current is generated in the second layer of the paper electrode compared to the cloth (i.e., for the paper-IDFF combination with two layers, 17% of the current is generated in the second layer, whereas this is 6% for the cloth-IDFF combination), the steep reduction in activation and mass transfer resistances (Figure 5f) results in a better performance output for two stacked cloth electrodes. The decrease in the activation (from 0.35 to $0.25 \text{ } \Omega \text{ cm}^2$) and mass transfer resistances (from 0.21 to $0.08 \text{ } \Omega \text{ cm}^2$) are partially related to the increase in internal surface area which counterbalances the negative effect of increased ohmic losses, resulting in a net performance gain of 56 mA cm^{-2} at 150 mV for two cloth electrodes. In addition, from the 1D profiles in Figure 6a–b, it is shown that the configuration with one cloth electrode distributes the current more homogeneously over the entire electrode thickness, as a result of the large through-plane pores, compared to one paper electrode, despite that the cloth electrode is twice as thick.

Further understanding is supported by the concentration plots obtained with the PNM (Figure 7). In the IDFF configuration, the electrolyte is pushed from the inlet to the outlet channel over the rib. Thus, by stacking electrodes, the ionic species transport pathway becomes larger, increasing the ionic resistance. Due to the homogeneous PSD of the paper electrode (Figure S5b), the pore-to-pore reactant depletion exhibits a uniform profile. Yet, in the region close to the membrane, the high reaction rates (Figure 6a) lead to greater reactant depletion,^[79] which is exacerbated in the IDFF by the poor species supply driven by the lower local velocities near the membrane (Figure 4b).^[59] Similar phenomena take place in the

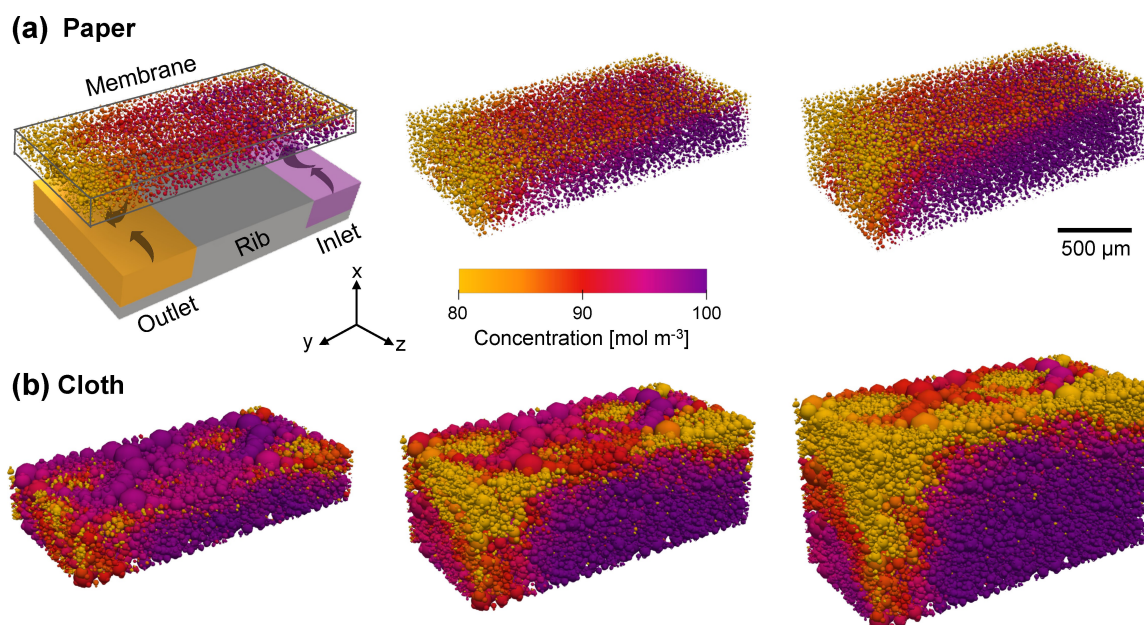


Figure 7. Concentration profiles of Fe^{3+} in the porous electrode using the interdigitated flow field (shown with a visual representation) obtained by pore network simulations at 3.5 cm s^{-1} and -0.2 V . The concentration profiles are shown for 1, 2 or 3 layers in thickness from left to right and for: (a) the paper electrode, and (b) the cloth electrode. The x-direction represents the thickness of the electrode from the flow field (bottom) to the membrane (top). The y-direction represents the length of the electrode and the z-direction the width.

electrode volume under the inlet and outlet channels, where the electrolyte convection is not as significant as under the ribs, resulting in stagnant zones due to preferential flow pathways. Consequently, stacking more carbon papers does not significantly improve the reactant distribution with IDFFs.

In the cloth electrode, the fluctuations in the normalized current distribution plot evince the heterogeneity of cloth materials.^[26,33] Their anisotropic microstructure with a bimodal PSD (Figure S5d) strongly affects the distribution of reactants,^[55] providing distinct concentration profiles in comparison to the paper electrode (Figure 7). A higher degree of local reactant depletion is found for the smaller pore segments with limited convective flow,^[35,92] anticipated by the electrolyte velocity distribution (Figure 4). Higher velocities are reached in the large pores, which enhance species transport in the in-plane direction when adding a second layer. Hence, alleviating the overall mass transfer overpotential and simultaneously the activation overpotential (Figure 5f) due to the greater accessibility of the specific surface area for the redox reactions. However, when an additional third layer is added, the increase in ohmic resistance counteracts the decrease in the activation and mass transfer overpotentials, and the overall electrochemical performance is no longer improved. We envision that modifying the through-plane microstructure of electrodes (i.e., gradients in porosity, pore size and morphology through new synthesis techniques and materials^[13,60,94]) shall enhance the electrolyte transport towards the membrane interface, increasing the reactant supply. Thereby, alleviating ohmic resistances and pressure losses in IDFF configurations, improving the electrolyte distribution and enabling the use of thicker electrodes with a high surface area.

Flow-Through Flow Field

Flow reactors with FTFFs induce a near unidirectional in-plane flow throughout the electrode structure as shown in the velocity distribution analysis (Figure 4c–d), especially for the paper electrode. The addition of a second electrode layer for FTFF configurations enhances the performance of both investigated electrode materials at the analyzed electrolyte velocity (Figure 5c–d), resulting in a 145 mA cm^{-2} increase for the paper electrode and a 73 mA cm^{-2} increase for the cloth electrode. The analysis of ohmic, activation and concentration overpotentials evidences a remarkable reduction in the activation and mass transfer resistances when adding a second layer, overcoming the negative impact of increased ohmic losses (Figure 5g–h). The main reasons for this reduction are the combination of the greater flow rate to maintain a constant electrolyte velocity, the increased internal surface area for the redox reactions, and the voids created between the stacked electrodes. However, further addition of a third layer no longer results in improved electrochemical performance, caused by no noticeable reduction in activation and mass transfer overpotentials. Further revealed by the current profiles in Figure 6c–d, where the reaction rate in the third layer is almost negligible compared to the first and second layers.

For the paper electrode, the performance gain with two layers is primarily defined by a decrease of $0.49 \text{ } \Omega \text{ cm}^2$ in the mass transfer resistance, ascribed to the greater flow rate resulting in higher non-reacted outlet concentrations and the increase in internal surface area. The high mass transfer overpotential in the paper-FTFF combination is caused by the lower mass transfer coefficient^[63] as a result of the unimodal PSD and long electrolyte flow pathway, impacting the mass transfer resistance at low flow rates. In contrast, for the cloth electrode, the performance improvement is dominated by a decrease of $0.37 \text{ } \Omega \text{ cm}^2$ in the activation overpotential as a result of the increased internal surface area when a second layer is added. Furthermore, the stacking of electrodes potentially enhances the electrode accessibility by better mixing across the large internal pores in the cloth electrode caused by the in-plane flow induced by the flow-through configuration (as shown in the velocity and concentration profiles of Figure 4d and Figure S12b, respectively).

Performance Trade-Off

The trade-off between the electrochemical performance and pressure losses should be evaluated to assess the influence of stacking electrodes on the overall flow cell performance. Therefore, in Figure 8 we compare the current density at an applied cell potential of 75 mV with the pressure drop per unit length for the different flow cell configurations with one, two and three electrode layers. It must be pointed out that we evaluate the trade-off for a single-electrolyte flow cell design to mitigate secondary effects such as membrane crossover or changes in the state-of-charge. Therefore, we applied a potential of 75 mV to a flow cell with an open-circuit voltage of 0 V, where the applied potential is equivalent to a voltage loss in a full-cell configuration. Thus, at a fixed applied potential in a single-electrolyte system, the aim is to maximize the current density at a given voltage for more efficient reactor operation. In Figure 8, each data point represents a distinct electrolyte velocity ($0.5, 1.5, 3.5$ and 5 cm s^{-1}) and the pumping requirements depend on the pressure drop and on the electrolyte flow rate ($P_p = (Q\Delta P/\eta_p)$ with P_p the pumping power (W), Q the flow rate ($\text{m}^3 \text{ s}^{-1}$), ΔP the pressure drop (Pa) and η_p the pumping efficiency (–)). Upon stacking electrode layers, higher electrolyte flow rates are necessary to ensure a constant electrolyte velocity and therefore, thicker electrodes may negatively impact the performance trade-off.

For most flow cell configurations, an optimum trade-off is achieved by stacking two electrode layers, dominated by a significant increase in electrochemical performance. When stacking more layers, dominant ohmic losses and elevated pumping requirements negatively impact the performance trade-off. Stacking electrode layers for the paper-IDFF does not augment the electrochemical performance, as observed in Figure 8a, whereas for the cloth-IDFF combination, the electrochemical performance is improved but this comes at the cost of a significantly increased pressure drop. Hence, the best trade-off for both electrodes with the IDFF is obtained for a single

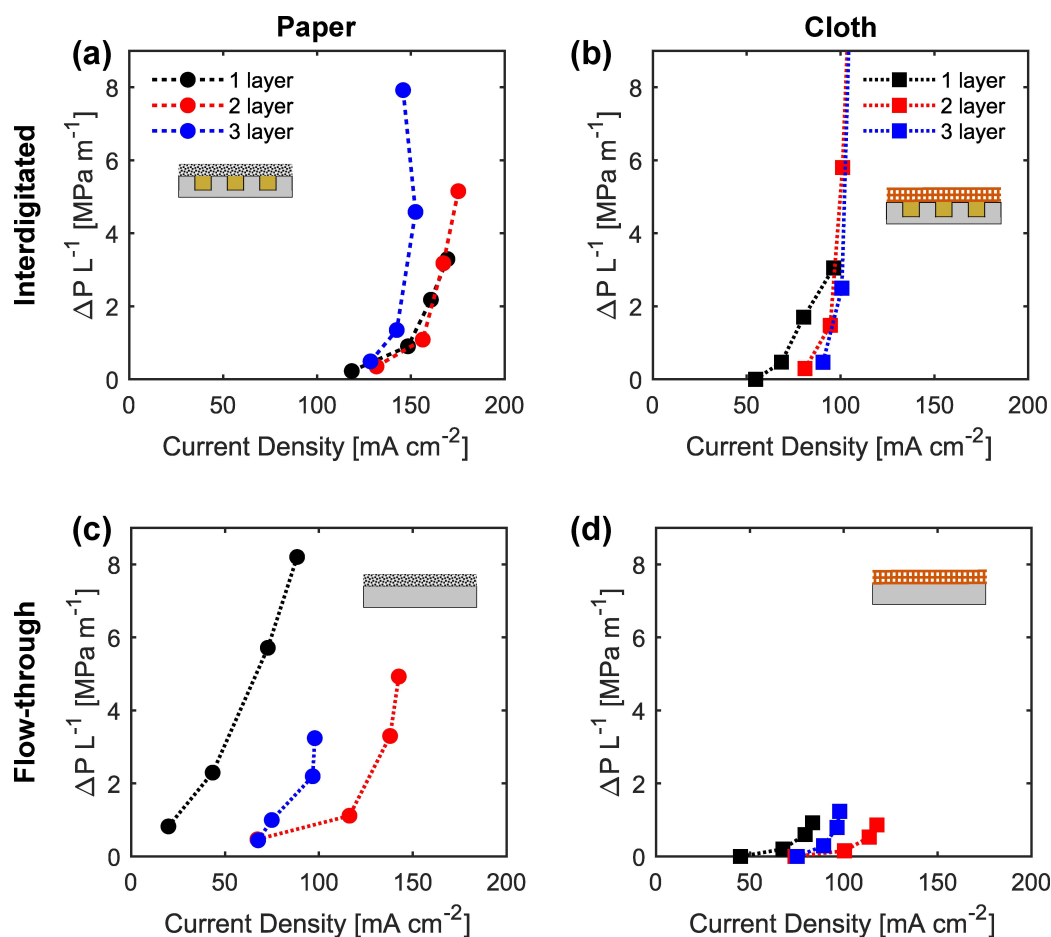


Figure 8. Balance between current density and pressure losses for the four electrode-flow field combinations with 1, 2 and 3 electrode layers, for the: (a) interdigitated flow field and paper electrode, (b) interdigitated flow field and cloth electrode, (c) flow-through flow field and paper electrode, and (d) flow-through flow field and cloth electrode. Each data point corresponds to a certain electrolyte velocity from 0.5 to 5 cm s⁻¹ and the current densities are compared at 75 mV cell potential.

electrode layer, as the expected material costs of stacking two electrode layers together with the high pumping power do not weigh against the increase in performance. For the FTFF, there is a significant performance gain in stacking two electrodes, as both the electrochemical performance and the associated pressure drop are improved (Figure 8c). Last, as anticipated, the cloth-FTFF combination features the lowest pressure drop, independent of the number of stacked layers, where the best trade-off is reached with two layers. Furthermore, we find that the optimum electrode layer thickness does not notably depend on the analyzed electrolyte velocity (each data point in Figure 8) for any of the flow cell designs.

When translating these findings to a broader context, we find that the optimal electrode thickness depends on the reactor design. For flow-through configurations, electrodes with a unimodal pore size distribution and high internal surface area feature significant species depletion across the electrode length because of the long residence time in the electrode. Therefore, thicker electrodes with a bimodal PSD with large pores, such as the cloth electrode, should be used as they facilitate a better electrolyte distribution at low pumping power. For interdigitated flow configurations on the other hand, an increased

internal surface area and a more uniform and smaller pore size distribution (e.g., the paper electrode) is beneficial as the residence time in the electrode is smaller. Combined with the hybrid in- and through-plane flow induced by this flow configuration, the best performance trade-off is found for thinner electrodes as the pressure drop decreases drastically. For carbon felts on the other hand, with unimodal PSDs with larger pores (60 μm),^[69] we expect that thicker electrodes (>200 μm) are beneficial in combination with both the IDFF and FTFF. However, as commercial felt electrodes are much thicker (2–6 mm), stacking commercial felt electrodes is anticipated to have a detrimental impact on the pressure losses, electrolyte maldistribution and ohmic losses associated with an increased ionic resistance. Furthermore, the redox chemistry will also play a role in the selection of the electrode thickness, where we anticipate that chemistries featuring sluggish kinetics will benefit from thicker electrodes due to the larger internal surface area, whereas electrolytes with facile redox kinetics will be less sensitive to an increase in electrode thickness.

Conclusions

The electrode thickness determines the flow battery performance through the available reaction surface area, the electrolyte distribution, and the ohmic, activation and mass transfer overpotentials. Increasing the electrode thickness by stacking commercial electrodes can be leveraged as a fast and inexpensive pathway to improve battery performance. While prior work investigated the influence of the electrode thickness in isolation from the type of flow field or electrode microstructure, here we systematically investigated the influence of the electrode thickness on the flow cell performance through electrode stacking of two commercial electrodes – Freudenberg paper and ELAT cloth – in combination with flow-through and interdigitated flow fields. We evaluated the electrochemical and fluid dynamic performance of the distinct flow cell designs using a series of polarization, electrochemical impedance spectroscopy and pressure drop measurements in a single-electrolyte cell configuration with an aqueous electrolyte ($\text{Fe}^{2+}/\text{Fe}^{3+}$ in HCl). Furthermore, we used pore network modeling to investigate the physicochemical phenomena occurring in the three-dimensional electrode microstructure and to understand local properties (e.g., concentration, current, pressure) besides the measurements performed in the analytical flow cell.

Using pressure drop measurements, we find that thicker electrodes in combination with flow-through flow fields decrease the pressure drop, which we attribute to hydraulic short-circuiting between the electrode layers. On the contrary, we find that for interdigitated flow fields, thinner electrodes are beneficial, which we hypothesize is because of the increase in pressure to push the electrolyte from the channel through the electrode at elevated flow rates. The electrochemical characterization shows the competing effects of reduced activation and mass transfer overpotentials with increased ohmic losses, which make the two-layer system (400–700 μm) the best configuration for almost all electrode-flow field combinations in terms of electrochemical performance. The paper-IDFF combination is however an exception to this trend, as no significant improvement is observed when more electrode layers are stacked. Furthermore, in the current distribution analysis from the PNM simulations, a negligible reaction rate was found in the third electrode layer, closest to the current collector, for all configurations. We find that the electrolyte velocity influences the electrode utilization, as under low electrolyte velocities (0.5 cm s^{-1}), more current is generated in the additional two and three layers because of increased reactant depletion as a result of low convection rates.

The narrow unimodal pore size distribution of the paper electrode adversely affects the benefits of increasing the electrode thickness in IDFF configurations, whereas the hierarchical anisotropic microstructure of the cloth electrode enhances the reactant replenishment. Consequently, the mass transfer resistance in the cloth electrode is reduced, enabling the electrolyte to access a greater electrode reaction volume through preferential pathways created by the larger pores. In the FTFF configuration, the impact of electrode thickness of specific electrode types on the electrochemical performance is

more remarkable than in the IDFF. In particular, the combination with two stacked paper electrodes offers a two times higher current density compared to two stacked cloth electrodes, driven by the higher current generation in the second layer enabled by the better electrolyte distribution due to the uniform microstructure of the paper electrode.

In this study, even though we found similarities in the number of stacked electrode layers for different systems, we demonstrated the critical dependency between the electrode-flow field interactions with the electrode thickness and their influence on different performance metrics (e.g., current distribution, pressure drop, electrolyte distribution) and corresponding system performance. When balancing the electrochemical performance with the associated pressure losses, thicker electrodes with a flow-through flow field are leveraged as a promising strategy to enhance the overall efficiency of the flow cell at low pressure drop, whereas thinner electrodes are beneficial with interdigitated flow fields.

Supporting Information

The authors have cited additional references [35,63,69,71,95,96] within the Supporting Information.

Author Contributions

V. Muñoz-Perales: conceptualization, methodology, validation, formal analysis, investigation, data curation, writing – original draft, writing – review & editing, visualization. **M. van der Heijden:** conceptualization, methodology, model validation, formal analysis, software, investigation, data curation, writing – original draft, writing – review & editing, visualization. **V. de Haas:** software, writing – review & editing. **J. Olinga:** data curation. **M. Vera:** writing – review & editing, funding acquisition. **A. Forner-Cuenca:** conceptualization, methodology, resources, writing – original draft, writing – review & editing, supervision, project administration, funding acquisition.

Acknowledgements

This work has been partially funded by the Agencia Estatal de Investigación (PID2019-106740RB-I00 and TED2021-129378B-C21/AEI/10.13039/501100011033). AFC gratefully acknowledges the Dutch Research Council (NWO) for financial support through the Talent Research Program Veni (17324). The authors are thankful to Rens Horst (Eindhoven University of Technology) for his constructive feedback on the manuscript.

Conflict of Interests

The authors declare no conflict of interest.

Data Availability Statement

The data that support the findings of this study are available from the corresponding author upon reasonable request.

Keywords: electrode thickness · flow field geometry · pore network modeling · porous electrode microstructure · redox flow batteries

- [1] A. A. Kebede, T. Kalogiannis, J. Van Mierlo, M. Berecibar, *Renewable Sustainable Energy Rev.* **2022**, *159*, 112213.
- [2] S. Chu, A. Majumdar, *Nature* **2012**, *488*, 294–303.
- [3] S. Koohi-Fayegh, M. A. Rosen, *J. Energy Storage* **2020**, *27*, 101047.
- [4] M. L. Perry, A. Z. Weber, *J. Electrochem. Soc.* **2016**, *163*, A5064–A5067.
- [5] P. Alotto, M. Guarnieri, F. Moro, A. Stella, *Int. J. Comput. Math. Electr. Electron. Eng.* **2013**, *32*, 1459–1470.
- [6] A. Z. Weber, M. M. Mench, J. P. Meyers, P. N. Ross, J. T. Gostick, Q. Liu, *J. Appl. Electrochem.* **2011**, *41*, 1137–1164.
- [7] E. Sánchez-Díez, E. Ventosa, M. Guarnieri, A. Trovò, C. Flox, R. Marcilla, F. Soavi, P. Mazur, E. Aranzabe, R. Ferret, *J. Power Sources* **2021**, *481*, 228804.
- [8] L. F. Arenas, C. Ponce de León, F. C. Walsh, *J. Energy Storage* **2017**, *11*, 119–153.
- [9] R. M. Darling, K. G. Gallagher, J. A. Kowalski, S. Ha, F. R. Brushett, *Energy Environ. Sci.* **2014**, *7*, 3459–3477.
- [10] S. Ha, K. G. Gallagher, *J. Power Sources* **2015**, *296*, 122–132.
- [11] J. Luo, A. P. Wang, M. Hu, T. L. Liu, *MRS Energy Sustainability* **2022**, *9*, 1–12.
- [12] X. Zhou, X. Zhang, L. Mo, X. Zhou, Q. Wu, *Small* **2020**, *16*, 1907333.
- [13] C. T. Wan, R. R. Jacquemond, Y. Chiang, K. Nijmeijer, F. R. Brushett, A. Forner-Cuenca, *Adv. Mater.* **2021**, *33*, 2006716.
- [14] C. T.-C. Wan, D. López Barreiro, A. Forner-Cuenca, J.-W. Barotta, M. J. Hawker, G. Han, H.-C. Loh, A. Masic, D. L. Kaplan, Y.-M. Chiang, F. R. Brushett, F. J. Martin-Martinez, M. J. Buehler, *ACS Sustainable Chem. Eng.* **2020**, *8*, 9472–9482.
- [15] S. Wang, X. Zhao, T. Cochell, A. Manthiram, *J. Phys. Chem. Lett.* **2012**, *3*, 2164–2167.
- [16] K. Lee, J. Lee, K. W. Kwon, M.-S. Park, J.-H. Hwang, K. J. Kim, *ACS Appl. Mater. Interfaces* **2017**, *9*, 22502–22508.
- [17] Y. Zeng, F. Li, F. Lu, X. Zhou, Y. Yuan, X. Cao, B. Xiang, *Appl. Energy* **2019**, *238*, 435–441.
- [18] B. Akuzum, Y. C. Alparslan, N. C. Robinson, E. Agar, E. C. Kumbur, *J. Appl. Electrochem.* **2019**, *49*, 551–561.
- [19] P. Geysens, Y. Li, I. Vankelecom, J. Fransaeer, K. Binnemans, *ACS Sustainable Chem. Eng.* **2020**, *8*, 3832–3843.
- [20] K. Gong, F. Xu, J. B. Grunewald, X. Ma, Y. Zhao, S. Gu, Y. Yan, *ACS Energy Lett.* **2016**, *1*, 89–93.
- [21] D. Aaron, Z. Tang, A. B. Papandrew, T. A. Zawodzinski, *J. Appl. Electrochem.* **2011**, *41*, 1175–1182.
- [22] R. Schweiss, C. Meiser, D. Dan, *Batteries* **2018**, *4*, 55.
- [23] Xiong Binyu, Zhao Jiyun, Li Jinbin, in *2013 IEEE Power Energy Soc. Gen. Meet.*, IEEE, Vancouver, BC, **2013**, pp. 1–5.
- [24] V. Muñoz-Perales, P. A. García-Salaberri, A. Mularczyk, S. E. Ibáñez, M. Vera, A. Forner-Cuenca, *J. Power Sources* **2023**, *586*, 233420.
- [25] W. Wang, Q. Luo, B. Li, X. Wei, L. Li, Z. Yang, *Adv. Funct. Mater.* **2013**, *23*, 970–986.
- [26] A. Forner-Cuenca, E. E. Penn, A. M. Oliveira, F. R. Brushett, *J. Electrochem. Soc.* **2019**, *166*, A2230–A2241.
- [27] C. R. Dennison, E. Agar, B. Akuzum, E. C. Kumbur, *J. Electrochem. Soc.* **2016**, *163*, A5163–A5169.
- [28] N. Aguiló-Aguayo, T. Drozdziak, T. Bechtold, *Electrochem. Commun.* **2020**, *111*, 106650.
- [29] M. D. R. Kok, R. Jervis, T. G. Tranter, M. A. Sadeghi, D. J. L. Brett, P. R. Shearing, J. T. Gostick, *Chem. Eng. Sci.* **2019**, *196*, 104–115.
- [30] J. Sun, M. C. Wu, X. Z. Fan, Y. H. Wan, C. Y. H. Chao, T. S. Zhao, *Energy Storage Mater.* **2021**, *43*, 30–41.
- [31] P. A. García-Salaberri, I. V. Zenyuk, A. D. Shum, G. Hwang, M. Vera, A. Z. Weber, J. T. Gostick, *Int. J. Heat Mass Transfer* **2018**, *127*, 687–703.
- [32] P. A. García-Salaberri, I. V. Zenyuk, G. Hwang, M. Vera, A. Z. Weber, J. T. Gostick, *Electrochim. Acta* **2019**, *295*, 861–874.
- [33] K. M. Tenny, A. Forner-Cuenca, Y.-M. Chiang, F. R. Brushett, *J. Electrochem. Energy Convers. Storage* **2020**, *17*, 041010.
- [34] A. A. Wong, M. J. Aziz, *J. Electrochem. Soc.* **2020**, *167*, 110542.
- [35] M. van der Heijden, R. van Gorp, M. A. Sadeghi, J. Gostick, A. Forner-Cuenca, *J. Electrochem. Soc.* **2022**, *169*, 040505.
- [36] Y. Su, H. Ren, S. Zhao, N. Chen, X. Wang, Y. Zhao, Y. Bai, C. Li, *Ceram. Int.* **2023**, *49*, 7761–7767.
- [37] R. Cervantes-Alcalá, M. Miranda-Hernández, *J. Appl. Electrochem.* **2018**, *48*, 1243–1254.
- [38] X. Ke, J. M. Prael, J. I. D. Alexander, J. S. Wainright, T. A. Zawodzinski, R. F. Savinell, *Chem. Soc. Rev.* **2018**, *47*, 8721–8743.
- [39] A. M. Pezeshki, R. L. Sacchi, F. M. Delnick, D. S. Aaron, M. M. Mench, *Electrochim. Acta* **2017**, *229*, 261–270.
- [40] S. Kumar, S. Jayanti, *J. Power Sources* **2016**, *307*, 782–787.
- [41] M. Messaggi, P. Canzi, R. Mereu, A. Baricci, F. Inzoli, A. Casalegno, M. Zago, *Appl. Energy* **2018**, *228*, 1057–1070.
- [42] T. Jyothi Latha, S. Jayanti, *J. Appl. Electrochem.* **2014**, *44*, 995–1006.
- [43] Q. Xu, T. S. Zhao, C. Zhang, *Electrochim. Acta* **2014**, *142*, 61–67.
- [44] R. M. Darling, M. L. Perry, *J. Electrochem. Soc.* **2014**, *161*, A1381–A1387.
- [45] Y. Wang, M. Li, L. Hao, *J. Electroanal. Chem.* **2022**, *918*, 116460.
- [46] J. Sun, B. Liu, M. Zheng, Y. Luo, Z. Yu, *J. Energy Storage* **2022**, *49*, 104135.
- [47] L. Wei, Z. X. Guo, J. Sun, X. Z. Fan, M. C. Wu, J. B. Xu, T. S. Zhao, *Int. J. Heat Mass Transfer* **2021**, *179*, 121747.
- [48] M. R. Gerhardt, A. A. Wong, M. J. Aziz, *J. Electrochem. Soc.* **2018**, *165*, A2625–A2643.
- [49] K.-Q. Zhu, Q. Ding, J.-H. Xu, Y.-R. Yang, C. Yang, J. Zhang, Y. Zhang, T.-M. Huang, W.-M. Yan, Z.-M. Wan, X.-D. Wang, *Energy Convers. Manage.* **2022**, *267*, 115915.
- [50] B. R. Chalamala, T. Soundappan, G. R. Fisher, M. R. Anstey, V. V. Viswanathan, M. L. Perry, *Proc. IEEE* **2014**, *102*, 976–999.
- [51] K. L. Duncan, K.-T. Lee, E. D. Wachsman, *J. Power Sources* **2011**, *196*, 2445–2451.
- [52] R. Banerjee, N. Bevilacqua, L. Eifert, R. Zeis, *J. Energy Storage* **2019**, *21*, 163–171.
- [53] Q. H. Liu, G. M. Grim, A. B. Papandrew, A. Turhan, T. A. Zawodzinski, M. M. Mench, *J. Electrochem. Soc.* **2012**, *159*, A1246–A1252.
- [54] D. S. Aaron, Q. Liu, Z. Tang, G. M. Grim, A. B. Papandrew, A. Turhan, T. A. Zawodzinski, M. M. Mench, *J. Power Sources* **2012**, *206*, 450–453.
- [55] H. Zhang, L. Zhu, H. B. Harandi, K. Duan, R. Zeis, P.-C. Sui, P. A. Chuang, *Energy Convers. Manage.* **2021**, *241*, 114293.
- [56] A. El-kharouf, T. J. Mason, D. J. L. Brett, B. G. Pollet, *J. Power Sources* **2012**, *218*, 393–404.
- [57] Z. Wang, J. Ren, J. Sun, Z. Guo, L. Wei, X. Fan, T. Zhao, *J. Power Sources* **2022**, *549*, 232094.
- [58] E. Ali, H. Kwon, J. Kim, H. Park, *J. Energy Storage* **2020**, *32*, 101802.
- [59] S. Tsushima, T. Suzuki, *J. Electrochem. Soc.* **2020**, *167*, 020553.
- [60] N. Misaghian, M. A. Sadeghi, K. M. Lee, E. P. L. Roberts, J. T. Gostick, *J. Electrochem. Soc.* **2023**, *170*, 070520.
- [61] J. Houser, J. Clement, A. Pezeshki, M. M. Mench, *J. Power Sources* **2016**, *302*, 369–377.
- [62] A. Z. Weber, M. M. Mench, J. P. Meyers, P. N. Ross, J. T. Gostick, Q. Liu, *J. Appl. Electrochem.* **2011**, *41*, 1137–1164.
- [63] J. D. Millshtein, K. M. Tenny, J. L. Barton, J. Drake, R. M. Darling, F. R. Brushett, *J. Electrochem. Soc.* **2017**, *164*, E3265–E3275.
- [64] K. V. Greco, A. Forner-Cuenca, A. Mularczyk, J. Eller, F. R. Brushett, *ACS Appl. Mater. Interfaces* **2018**, *10*, 44430–44442.
- [65] P. K. Weissenborn, R. J. Pugh, *J. Colloid Interface Sci.* **1996**, *184*, 550–563.
- [66] A. Forner-Cuenca, E. E. Penn, A. M. Oliveira, F. R. Brushett, *J. Electrochem. Soc.* **2019**, *166*, A2230.
- [67] M. A. Sadeghi, M. Aganou, M. Kok, M. Aghighi, G. Merle, J. Barralet, J. Gostick, *J. Electrochem. Soc.* **2019**, *166*, A2121–A2130.
- [68] D. Zhang, A. Forner-Cuenca, O. O. Taiwo, V. Yufit, F. R. Brushett, N. P. Brandon, S. Gu, Q. Cai, *J. Power Sources* **2020**, *447*, 227249.
- [69] A. Forner-Cuenca, E. E. Penn, A. M. Oliveira, F. R. Brushett, *J. Electrochem. Soc.* **2019**, *166*, A2230–A2241.
- [70] I. Derr, M. Bruns, J. Langner, A. Fetyan, J. Melke, C. Roth, *J. Power Sources* **2016**, *325*, 351–359.
- [71] N. Meddings, M. Heinrich, F. Overney, J.-S. Lee, V. Ruiz, E. Napolitano, S. Seitz, G. Hinds, R. Raccichini, M. Gaberšček, J. Park, *J. Power Sources* **2020**, *480*, 228742.
- [72] G. Paasch, K. Micka, P. Gersdorf, *Electrochim. Acta* **1993**, *38*, 2653–2662.
- [73] J.-B. Jorcin, M. E. Orazem, N. Pébère, B. Tribollet, *Electrochim. Acta* **2006**, *51*, 1473–1479.

- [74] J. D. Milshtein, J. L. Barton, R. M. Darling, F. R. Brushett, *J. Power Sources* **2016**, *327*, 151–159.
- [75] J. T. Gostick, *Phys. Rev. E* **2017**, *96*, 023307.
- [76] M. van der Heijden, A. Forner-Cuenca, *Encycl. Energy Storage* **2022**, 480–499.
- [77] A. Forner-Cuenca, F. R. Brushett, *Curr. Opin. Electrochem.* **2019**, *18*, 113–122.
- [78] V. Muñoz-Perales, M. Van Der Heijden, P. A. García-Salaberri, M. Vera, A. Forner-Cuenca, *ACS Sustainable Chem. Eng.* **2023**, *11*, 12243–12255.
- [79] J. Shokri, D. Niblett, M. Babaei, V. Niasar, *J. Electrochem. Soc.* **2022**, *169*, 120511.
- [80] E. Nishikata, T. Ishii, T. Ohta, *J. Chem. Eng. Data* **1981**, *26*, 254–256.
- [81] K. L. Hawthorne, J. S. Wainright, R. F. Savinell, *J. Electrochem. Soc.* **2014**, *161*, A1662–A1671.
- [82] Z. Galus, R. N. Adams, *ACS Publ.* **1963**, *67*, 866–871.
- [83] B. K. Chakrabarti, E. Kalamaras, A. K. Singh, A. Bertei, J. Rubio-García, V. Yufit, K. M. Tenny, B. Wu, F. Tariq, Y. S. Hajimolana, N. P. Brandon, C. T. John Low, E. P. L. Roberts, Y.-M. Chiang, F. R. Brushett, *Sustain. Energy Fuels* **2020**, *4*, 5433–5468.
- [84] A. Fathiganjehlou, A. Eghbalmanesh, M. W. Baltussen, E. A. J. F. Peters, K. A. Buist, J. A. M. Kuipers, *Chem. Eng. Sci.* **2023**, *273*, 118626.
- [85] A. Lenci, F. Zeighami, V. Di Federico, *Transp. Porous Media* **2022**, *144*, 459–480.
- [86] M. Van Der Heijden, M. Kroese, Z. Borneman, A. Forner-Cuenca, *Adv. Mater. Technol.* **2023**, *8*, 2300611.
- [87] A. Tang, J. Bao, M. Skyllas-Kazacos, *J. Power Sources* **2014**, *248*, 154–162.
- [88] N. M. Delgado, R. Monteiro, M. Abdollahzadeh, P. Ribeirinha, A. Bentien, A. Mendes, *J. Power Sources* **2020**, *480*, 229142.
- [89] B. Segel, Z. Parr, T. V. Sawant, C. S. Yim, D. M. Miller, T. J. Henry, J. R. McKone, *J. Mater. Chem. A* **2022**, *10*, 13917–13927.
- [90] E. B. Boz, P. Boillat, A. Forner-Cuenca, *ACS Appl. Mater. Interfaces* **2022**, *14*, 41883–41895.
- [91] A. A. Shah, M. J. Watt-Smith, F. C. Walsh, *Electrochim. Acta* **2008**, *53*, 8087–8100.
- [92] R. van Gorp, M. van der Heijden, M. Amin Sadeghi, J. Gostick, A. Forner-Cuenca, *Chem. Eng. J.* **2022**, 139947.
- [93] M. Skyllas-Kazacos, M. Kazacos, *J. Power Sources* **2011**, *196*, 8822–8827.
- [94] L. F. Arenas, C. Ponce de León, F. C. Walsh, *Electrochem. Commun.* **2017**, *77*, 133–137.
- [95] K. T. Cho, P. Ridgway, A. Z. Weber, S. Haussener, V. Battaglia, V. Srinivasan, *J. Electrochem. Soc.* **2012**, *159*, A1806–A1815.
- [96] V. Muñoz-Perales, S. E. Ibáñez, E. García-Quismondo, S. Berling, M. Vera, **2023**, DOI 10.26434/chemrxiv-2023-13q43.

Manuscript received: August 1, 2023

Revised manuscript received: October 23, 2023

Version of record online: December 27, 2023